

Low-Mode Internal Tide Propagation in a Turbulent Eddy Field

MICHAEL DUNPHY, AURÉLIEN L. PONTE, PATRICE KLEIN,^a AND SYLVIE LE GENTIL

University of Brest, CNRS, IRD, Ifremer, Laboratoire d'Océanographie Physique et Spatiale, IUEM, Brest, France

(Manuscript received 21 April 2016, in final form 10 December 2016)

ABSTRACT

Understanding and predicting how internal tides distort and lose coherence as they propagate through the ocean has been identified as a key issue for interpreting data from the upcoming wide-swath altimeter mission Surface Water and Ocean Topography (SWOT). This study addresses the issue through the analysis of numerical experiments where a low-mode internal tide propagates through a quasigeostrophic turbulent jet. Equations of motion linearized around the slower turbulent field are projected onto vertical modes and assumed to describe the dynamics of the low-mode internal tide propagation. Diagnostics of the terms responsible for the interaction between the wave and the slow circulation are computed from the numerical outputs. The large-scale change of stratification, on top of eddies and jet meanders, contributes significantly to these interaction terms, which is shown to be consistent with an independent scaling analysis. The sensitivity of interaction terms to a degradation of the slow field spatial and temporal resolution indicates that present-day observing systems (Argo network, altimetry) may lack the spatial resolution necessary to correctly predict internal tide evolution. The upcoming SWOT satellite mission may improve upon this situation. The number of vertical modes required to properly estimate interaction terms is discussed. These results advocate development of a simplified model based on solving a modest number of the linearized equations subject to a prescribed mesoscale field and internal tide sources.

1. Introduction

Oceanic internal tides (IT) are internal waves generated when barotropic tidal currents encounter topographic slopes and perturb the oceanic stratification (Garrett and Kunze 2007). When superinertial, the internal waves thereby produced are free to propagate across oceans. The signature of IT on sea level may be extracted from altimetric observations, and amplitudes of up to 5 cm have been found (Ray and Zaron 2011). A prerequisite condition to this extraction is that IT maintain a fixed-phase relationship with astronomical forcing over the period of time required by the analysis, which is of the order 3 yr. It has become clear that a significant part of IT loses such phase relationship and are called “incoherent” as, while propagating, they encounter mesoscale eddies, which

populate oceans (Zaron and Egbert 2014; Shriver et al. 2014; Kerry et al. 2014; Zaron 2015). Incoherent IT and internal waves in general have been identified as a critical issue to the interpretation of high-resolution altimetric data, which will be obtained thanks to the upcoming Surface Water and Ocean Topography (SWOT) mission (Arbic et al. 2015; Klein et al. 2015; Dufau et al. 2016). The issue posed by IT arises from the need to distinguish IT and slower balanced contributions in order to diagnose the ocean circulation. The problem is difficult because (i) the IT and internal waves contribute sea surface height signals in the 10–100-km wavelength band, which superimpose on the signals from submesoscale and mesoscale circulation (Richman et al. 2012; Rocha et al. 2016), and (ii) the long revisit time of altimeters (order 10 days) prohibits removing the waves by temporal averaging. Consequently, the IT and balanced signatures are entangled in the altimetric data. The development of realistic IT resolving numerical simulations of the ocean circulation (Arbic et al. 2010) may help in isolating the IT contribution in high-resolution altimetric data. The cost of such simulations

^a Current affiliation: California Institute of Technology, and Jet Propulsion Laboratory, NASA, Pasadena, California.

Corresponding author e-mail: Michael Dunphy, mdunphy@uwaterloo.ca

complicates the data assimilation required to produce accurate forecasts. An alternative road is taken here that consists of dynamically inspecting the propagation of IT through a turbulent eddy field in an idealized numerical simulation. The underlying motivation is to investigate whether a simplified model of IT propagation could be designed. How should this model be expressed conceptually? What accuracy in terms of resolution of the background circulation is required in order to correctly predict the IT?

Several theoretical frameworks have been developed to describe interactions between internal gravity waves and slower quasigeostrophic motions. The propagation of small-scale internal waves into a larger-scale background is amenable to a ray tracing approach, which led to the identification of the “wave capture” mechanism (Bühler and McIntyre 2005; Plougonven and Snyder 2005; Polzin 2010). Spatial-scale separation is not justified in general when the wave is near-inertial or has a low-mode vertical structure.¹ Young and Ben Jelloul (1997) leveraged the separation of time scales between near-inertial internal waves and a slowly evolving background to develop a theoretical framework that predicts the evolution of the near-internal, wave-demodulated amplitude. The approach was also used to predict the concentration of near-inertial waves in anticyclones (Danioux et al. 2015). Near-inertial waves stronger than geostrophic eddies affect the evolution of the slower flow, and Xie and Vanneste (2015) developed a theoretical framework that describes the joint evolution of both types of motions. Wagner and Young (2016) developed, under the same assumption, a three-component model describing the coupled evolution of near-inertial waves, the slow-flow, and the near-inertial second harmonic waves (i.e., those near twice the local inertial frequency). The authors showed that these harmonics, even though small, actively participate in the cascade of near-inertial waves to smaller scales. A critical assumption of these theoretical models that focus on near-inertial internal waves is the small Burger number assumption, which translates to the slow propagation of near-inertial waves $[\text{Bu} = (H_w/L_w \times N/f)^2 = \tilde{\omega}^2 - 1,$

where N and f are the buoyancy and Coriolis frequencies]. The assumption does not hold for low-mode internal tides away from the inertial latitude. Ward and Dewar (2010) thus used triad interaction theory in a single-layer, shallow-water setting to quantify the directional spreading of a wave interacting with geostrophic turbulence. Short waves were found to spread faster and in a narrower cone defined by the wave propagation direction than longer (more inertial) waves and that strengthening the turbulence increased the pace of the spreading. Using a multiple time-scale expansion and the method of reconstitution, Wagner (2016) derived an equation predicting the simultaneous evolution of an internal wave with unit Burger number and a balanced flow, assuming both are of comparable magnitudes. Wagner (2016) provides an extension of Young and Ben Jelloul (1997) to more general internal waves. The conceptual framework derived here relies on the weakness of the internal waves, such that linearized equations of motion are expected to describe the internal wave evolution while neglecting feedback on the slow flow.

Other efforts resorted to numerical modeling. Dunphy and Lamb (2014) propagated a mode-one internal tide through geostrophic eddies, finding that barotropic eddies distorted the incident wave, while baroclinic eddies scattered a portion of the incident wave to higher vertical modes. Zaron and Egbert (2014) employed a realistic model near the Hawaiian Archipelago, including both tidal forcing and the evolution of the slower background circulation. Zaron and Egbert (2014) focused on the low vertical-mode dynamics and interpreted variability of the internal tide response in terms of phase speed variability. Three sources of variability were identified: refraction due to change of the background stratification, Doppler shifting (proportional to a mixed Froude number), and refractions due to the background vorticity (proportional to a Rossby number). Background stratification was found to be the largest of the three. The present work builds upon Zaron and Egbert (2014) by identifying the nature of the vertical-mode coupling between slow and fast fields via projections of equations of motions onto vertical modes.

In this paper, we consider the interaction between quasigeostrophic turbulence and a low-mode internal tide. Low modes contribute most significantly to sea level fluctuations (Ray and Zaron 2011), hence this choice of focus. Section 2 describes the numerical experiment, and section 3 describes the analytical framework. Results are presented in section 4,

¹ Use of the internal gravity wave dispersion relation leads to $L_w/L_g = (H_w/H)/\sqrt{\tilde{\omega}^2 - 1} \times (L_d/L_g)$, where L_w and H_w are the inverses of horizontal and vertical wavenumbers, $\tilde{\omega}$ is the ratio of the wave frequency to the Coriolis frequency, L_g is the horizontal length scale associated with slow motions, L_d is the baroclinic Rossby radius of deformation, and H is the flow depth.

TABLE 1. Parameters used in the ROMS simulations.

Parameter	Value	Description
T	12 h	Tidal period
$L_x \times L_y \times H$	1024 km \times 2880 km \times 4 km	Domain dimensions
$\Delta x \times \Delta y, N_z, \Delta t$	4 km \times 4 km, 50 levels, 300 s	Space and time resolution ($t \leq 1500$ d)
$\Delta x \times \Delta y, N_z, \Delta t$	2 km \times 2 km, 100 levels, 150 s	Space and time resolution ($t > 1500$ d)
f_0	$1.0313 \times 10^{-4} \text{ s}^{-1}$	Coriolis parameter
β	$1.6186 \times 10^{-11} \text{ m}^{-1} \text{ s}^{-1}$	Beta parameter
$f(y)$	$f_0 + \beta y, y \in [-L_y/2, L_y/2]$	Local rotation rate
y_{jet}	800 km	Jet width
r_d	$H/(100 \text{ days})$	Linear bottom drag coefficient

and conclusions and a discussion are found in [section 5](#).

2. Numerical experiment

We use the numerical model Regional Oceanic Modeling System (ROMS; see [Shchepetkin and McWilliams 2005](#)) to propagate a mode-one internal tide through a turbulent quasigeostrophic field. The domain is a zonally periodic, constant-depth rectangular region on a β plane with closed north and south boundaries. [Table 1](#) lists the parameters.

We initialize the density with north and south density profiles in the north and south halves of the domain, respectively. The profiles are those of [Klein et al. \(2008\)](#). At the center, we smoothly blend the profiles over a width y_{jet} , forming a meridional density gradient that supports an unstable zonal jet. Last, adding a small perturbation starts the instability.

The experiments begin with a spinup phase and conclude with an interaction phase. The spinup runs for 1500 days at low resolution (4 km, 50 vertical levels) and continues for 500 days at higher resolution (2 km, 100 vertical levels). The nonuniform vertical resolution increases from 190 m near the bottom to 3.6 m near the surface and well resolves the low-mode features that are the focus of this study. During the spinup phase the unstable jet produces quasigeostrophic turbulence and is powered by the energy held in the meridional density gradient. To maintain the density gradient, we restore the zonal mean (ZM) of density, velocity, and sea level toward the unperturbed initial conditions on a 100-day time scale. A linear bottom drag with coefficient r_d is applied (corresponding to the same 100-day time scale), which acts to damp the turbulent field.

At $t = 2000$ days, we suspend the zonal mean restoring and switch on mode-one internal tide forcing 400 km from the southern boundary. The slow turbulence spins down, while the forced waves propagate

both northward and southward from the forcing location. Sponge regions remove waves as they approach the closed north and south boundaries. The interactions between the northward-propagating waves and the quasigeostrophic field are the focus of this experiment.

3. Analytical framework

a. Tidal slow decomposition

Internal tide and slow contributions are separated using temporal filters. A sliding average extracts the slow part of the dynamical variables

$$\bar{a} = \frac{1}{2T} \int_{t-2T}^t a(t') dt', \quad (1)$$

where T is the tidal period, and we identify these fields as the slow quasigeostrophic part (overbar notation). Harmonic fits at the tidal frequency $\omega_0 = 2\pi/T$ extract the fast tidal frequency wave part (circumflex notation):

$$\hat{a}^{\cos} = \frac{1}{T} \int_{t-2T}^t a(t') \cos \omega_0 t' dt', \quad \text{and} \quad (2)$$

$$\hat{a}^{\sin} = \frac{1}{T} \int_{t-2T}^t a(t') \sin \omega_0 t' dt'. \quad (3)$$

We conduct temporal separation online with ROMS and store averages, harmonic fits, and instantaneous snapshots of the dynamic variables u, v, w, ρ , and η . During the interaction phase fields are saved every 25 days, except for the period where $t \in [3000, 3050]$ days, where we output each day. ROMS uses a time-varying vertical coordinate that conforms to the sea surface height; during offline analysis we interpolate the saved fields to a nominal vertical coordinate corresponding to zero sea surface height.

[Figure 1](#) shows the zonal mean of slow density anomaly $\bar{\rho}$ and slow zonal velocity \bar{u} at $t = 3000$ days.

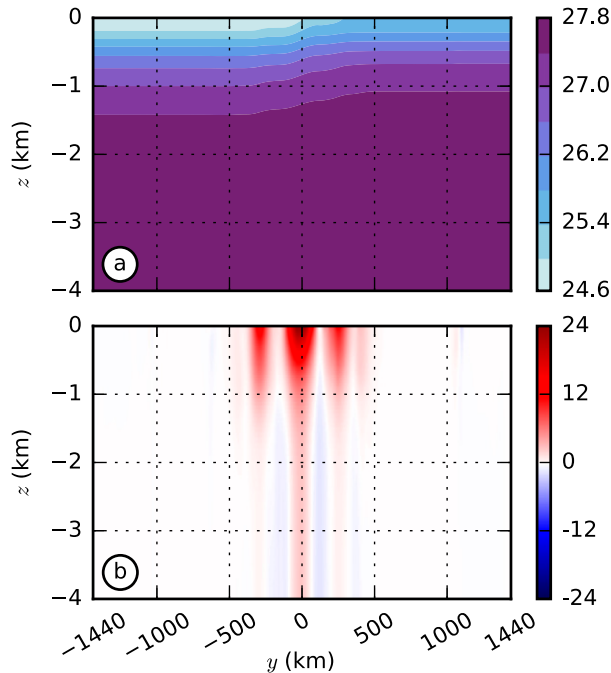


FIG. 1. Zonal mean of (a) slow density anomaly $\bar{\rho}$ (kg m^{-3}) and (b) slow zonal velocity \bar{u} (cm s^{-1}) at $t = 3000$ days.

The meridional density gradient and slow zonal jets are constrained to the zonal band bounded by $y = \pm 500$ km. Figure 2 shows a plan view of the model domain colored by the slow and fast sea surface height ($\bar{\eta}$ and $\hat{\eta}$) at $t = 3000$ days and also shows the internal tide forcing and sponge regions.

b. Tidal dynamics

We assume the propagation of the IT throughout the turbulent eddy field is well approximated by the hydrostatic primitive equations linearized about the slow flow, which is assumed to be known. This linearization relies on the assumption that internal tide fluctuations are weak compared to that of the slow flow (Bühler 2014). Feedback of internal waves on the slow flow and interactions with higher harmonics (e.g., with $2\omega_0$ frequency) are ignored, and that may limit the relevance of the approach on long time scales. Additionally, the buoyancy equation is integrated vertically to obtain an equation for pressure, which results in the following set of equations:

$$\partial_t \hat{\mathbf{u}}_h + (\hat{\mathbf{u}} \cdot \nabla) \bar{\mathbf{u}}_h + (\bar{\mathbf{u}} \cdot \nabla) \hat{\mathbf{u}}_h + f \mathbf{k} \times \hat{\mathbf{u}}_h = -\nabla \hat{p}, \quad (4)$$

$$\partial_t (\hat{p} - g \hat{\eta}) - \int_z^0 [(\hat{\mathbf{u}} \cdot \nabla) \bar{b} + (\bar{\mathbf{u}} \cdot \nabla) \hat{b} + \hat{w} N^2] dz' = 0, \quad (5)$$

$$\partial_z \hat{p} = \hat{b}, \quad \text{and} \quad (6)$$

$$\nabla \cdot \hat{\mathbf{u}} = 0, \quad (7)$$

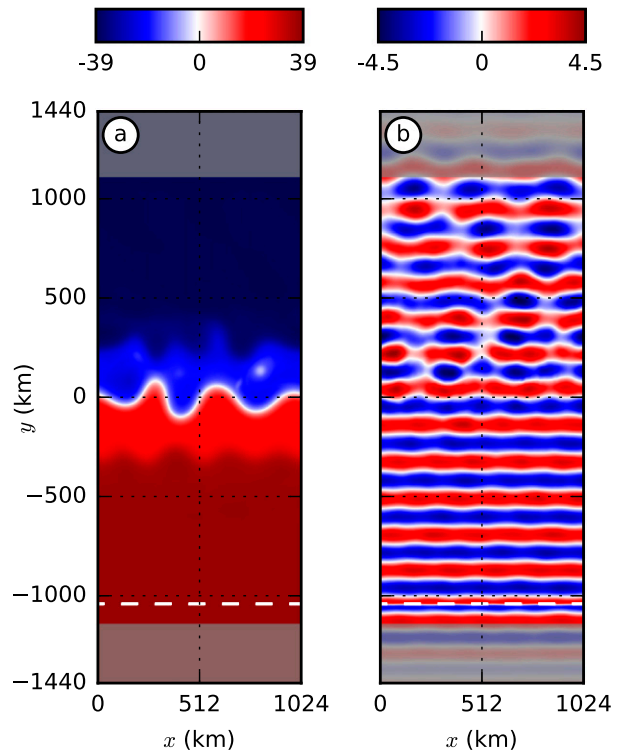


FIG. 2. Overview of the computational domain, colored by sea surface height (cm) at $t = 3000$ days, showing (a) $\bar{\eta}$, the slow quasigeostrophic part, and (b) $\hat{\eta}$, the fast wave part. The dashed white line shows the position of the internal wave forcing, and the shaded parts indicate relaxation regions.

where $\hat{\cdot}$ designates $\hat{\cdot}^{\cos}$ or $\hat{\cdot}^{\sin}$, where $\mathbf{u} = (u, v, w)$ and $\mathbf{u}_h = (u, v)$ are the three-dimensional and horizontal velocity vectors, respectively, where \mathbf{k} is the unit vector in the z dimension, b is buoyancy, and p is pressure. Where a quasigeostrophic field is not present, the equations simply support propagating linear internal waves. Nonlinear interaction terms between the IT and the eddy field have two components. The first represents refractive effects, that is, the advection of the slow flow by the waves, while the second represents advective or Doppler effects, that is, the advection of the waves by the slow flow.

c. Vertical modes

With a horizontally uniform background buoyancy frequency $N(z)$, we can expand the flow fields onto a vertical-mode basis following

$$(u, v, p) = \sum_{n=0}^{\infty} (u_n, v_n, p_n) \phi_n(z), \quad \text{and} \quad (8)$$

$$w = \sum_{n=0}^{\infty} \frac{w_n}{N^2(z)} \frac{d}{dz} \phi_n(z), \quad (9)$$

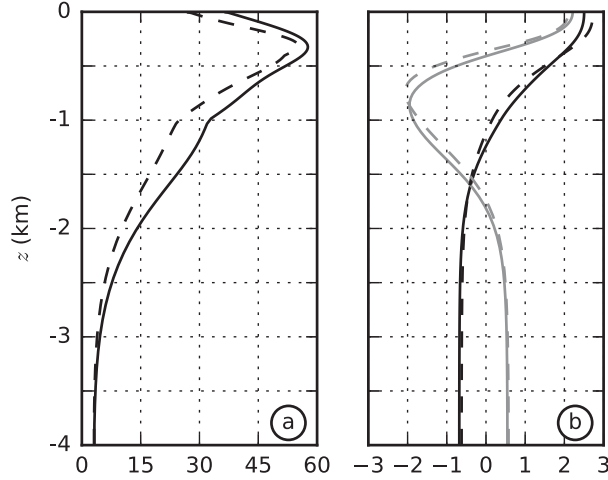


FIG. 3. Comparison between the north (solid) and south (dashed) stratification, showing (a) $N(z)/f_0$ and (b) vertical-mode functions $\phi_l(z)$ (black) and $\phi_2(z)$ (gray).

where the vertical-mode functions $\phi_n(z)$ that form an orthonormal basis satisfy the Sturm–Liouville problem (Gill 1982)

$$\frac{d}{dz} \left[\frac{1}{N^2(z)} \frac{d}{dz} \phi_n \right] + \frac{1}{c_n^2} \phi_n = 0, \quad (10)$$

subject to free surface and flat bottom conditions

$$g \frac{d}{dz} \phi_n + N^2(z) \phi_n = 0 \quad \text{at } z = 0, \quad \text{and} \quad (11)$$

$$\frac{d}{dz} \phi_n = 0 \quad \text{at } z = -H, \quad (12)$$

where c_n is the eigenvalue, and g is the gravitational acceleration constant. Each pair of ϕ_n and ϕ_m satisfy the inner product

$$\langle \phi_n \phi_m \rangle = \frac{1}{H} \int_{-H}^0 \phi_n \phi_m dz = \delta_{nm}, \quad (13)$$

and the projection coefficients are

$$(u_n, v_n, p_n) = \langle (u, v, p) \phi_n \rangle, \quad \text{and} \quad (14)$$

$$w_n = c_n^2 \nabla_h \cdot \mathbf{u}_{h,n}. \quad (15)$$

The southern and northern stratification and associated first two baroclinic modes are shown in Fig. 3 and indicate some differences whose importance will be discussed in more detail in section 4b.

d. Modally projected equations

Taking the inner product [(13)] between the linearized equations [(4)–(7)] and $\phi_n(z)$ yields projected equations for each wave mode n :

$$\partial_t \hat{u}_n - f \hat{v}_n + \partial_x \hat{p}_n = I_n^u(\hat{\mathbf{u}}, \bar{\mathbf{u}}), \quad (16)$$

$$\partial_t \hat{v}_n + f \hat{u}_n + \partial_y \hat{p}_n = I_n^v(\hat{\mathbf{u}}, \bar{\mathbf{u}}), \quad (17)$$

$$\partial_t \hat{p}_n + c_n^2 \nabla_h \cdot \hat{\mathbf{u}}_{h,n} = I_n^p(\hat{\mathbf{u}}, \bar{\mathbf{u}}, \hat{p}, \bar{p}), \quad (18)$$

$$\hat{w}_n = c_n^2 \nabla_h \cdot \hat{\mathbf{u}}_{h,n}, \quad \text{and} \quad (19)$$

$$\hat{p}_n = \hat{b}_n, \quad (20)$$

where the expressions for interaction terms I_n^u , I_n^v , and I_n^p are given in appendix A. The interaction terms gather the general couplings between any wave mode m and any slow mode l . Each coupling is weighted by the wave- and slow-mode field projections as well as coupling coefficients ($\alpha_{n,m,l}$, $\beta_{n,m,l}$, $\gamma_{n,m,l}$, or $\delta_{n,m,l}$) that describe how strongly the vertical coupling between mode m and mode l projects onto mode n . In our analysis, we truncate the sums at the limits $M = L = 8$ (see appendix A), which is enough to capture the most energetic vertical modes (see section 4).

e. Scaling analysis

To assess the amplitude of the interaction terms, we assume that slow and tidal fields scale according to

$$\begin{aligned} \nabla \cdot \bar{\mathbf{u}}_{h,l} &\sim U_g/L_g, & \nabla \cdot \hat{\mathbf{u}}_{h,n} &\sim U_w/L_w, \\ \bar{w}_l &\sim Rc_l^2 U_g/L_g, & \hat{w}_n &\sim c_n^2 U_w/L_w, \\ \bar{p}_l &\sim f_0 U_g L_g, & \hat{b}_n \sim \hat{p}_n &\sim (1 - \tilde{\omega}^{-2}) \omega_0 U_w L_w, \\ f &\sim f_0, & t &\sim 1/\omega_0, \end{aligned}$$

where the slow vertical velocity follows a typical quasigeostrophic scaling (Vallis 2006), where the internal wave polarization is used to scale the fast pressure and where two nondimensional parameters appear:

$$R = \frac{U_g}{f_0 L_g}, \quad \tilde{\omega} = \frac{\omega_0}{f_0}.$$

These correspond to the Rossby number of the slow flow ($\ll 1$) and the order-one frequency ratio ($\tilde{\omega} \sim 1.4$). Note that the dispersion relation for the internal wave links the frequency, wavelength, eigenvalue, and Coriolis parameter and is given in nondimensional form as $1 - \tilde{\omega}^{-2} = c_n^2/L_w^2 \omega_0^2$.

The scaling of the momentum and pressure interaction terms is presented in appendix B. For a mode-one incident wave, the projected momentum equations [(16) and (17)] scale as

$$\underbrace{\partial_t \hat{\mathbf{u}}_{h,1}}_{(1)} + \underbrace{f \times \hat{\mathbf{u}}_{h,1}}_{(\tilde{\omega}^{-1})} + \underbrace{\nabla \hat{p}_1}_{(1 - \tilde{\omega}^{-2})} = \underbrace{I_1^{u,v}}_{[R \tilde{\omega}^{-1} \max(1, \mu)]}, \quad (21)$$

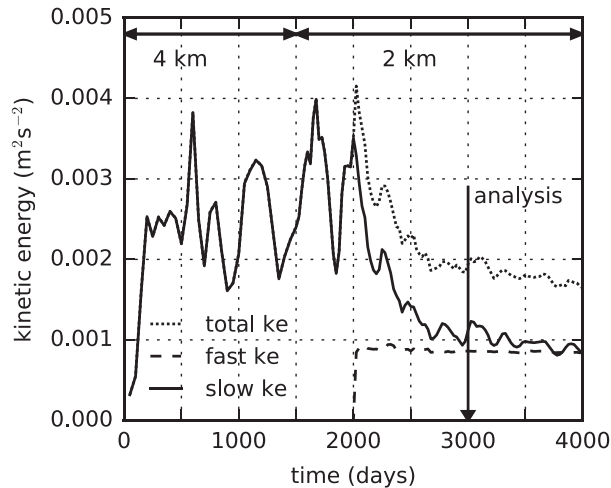


FIG. 4. Horizontal kinetic energy density computed from snapshots (dotted), slow fields (solid), and harmonic fits (dashed) averaged over the zonal band bounded by $y = \pm 500$ km. The resolution is doubled at $t = 1500$ days. At $t = 2000$ days the restoring is turned off and internal tide forcing switched on.

and the projected pressure equation [(18)] scales as

$$\underbrace{\frac{\partial_p \bar{p}_1}{(1)}} + \underbrace{\frac{c_1^2 \nabla_h \cdot \bar{\mathbf{u}}_{h,1}}{(1)}} = \underbrace{\frac{P_1}{[R\mu/(\tilde{\omega}^2 - 1) \max(1, \mu)]}} \quad (22)$$

where each term is normalized by the trend term scaling, and the horizontal length-scale ratio $\mu = L_g/L_w$ appears as the third nondimensional parameter. The frequency dependency is retained in order to account for the near-unity value of $\tilde{\omega}$, and it plays a modest role as $\tilde{\omega}^{-1} \sim 0.7$, $1 - \tilde{\omega}^{-2} \sim 0.5$, and $\tilde{\omega}^2 - 1 \sim 1$. From this analysis, we expect the interaction terms to scale linearly with the slow-flow Rossby number. When the slow flow has scales larger than the incident internal wave, we expect the interactions to further scale with the length-scale ratio μ —linearly in the momentum equations and quadratically in the pressure equation. An evaluation of the scaling analysis performance, including a summary of the range of values for U_g , L_g , and the nondimensional parameters, is presented in section 4g.

4. Results

This section presents results from the numerical simulations described in section 2. We begin with a look at the temporal separation into slow and fast components, followed by an assessment in terms of vertical modes and projected momentum–pressure balances. Last, we approximate the slow–fast interaction terms to probe the sensitivity of their construction subject to an incomplete slow field description.

We restrict analysis to the region truncated at $y = \pm 1000$ km in order to exclude the forcing and sponge regions.

a. Frequency filtering

The energy levels in the experiment vary as the simulation proceeds. Figure 4 shows the horizontal kinetic energy density computed from the instantaneous snapshots, average fields, and harmonic fits. The early part of the spinup phase ($t < 200$ days) reveals a rapid increase in slow kinetic energy as the turbulent field forms. During the remainder of the spinup the turbulent field evolves subject to restoring of the zonal mean quantities to initial conditions. The energy of the slow (i.e., 1-day averaged) fields matches well with that of the instantaneous snapshots, suggesting that there is little fast energy associated with the turbulent jet.

Restoring ceases and internal tide forcing begins at $t = 2000$ days. The energy in the slow fields decays in a spindown process as the bottom drag parameterization removes energy. It takes about 10 days for the mode-one internal tide to propagate across the domain meridionally, and the fast kinetic energy thus reaches a quasi-steady level.

We extracted “synthetic mooring” time series data at two locations: the first in the center of the domain, where the jet is present, and the second to the north beyond the geostrophic turbulence. Using this data, we integrated the horizontal velocity spectrum over each harmonic of the forcing frequency ω_0 . At both locations, energy at $2\omega_0$ was three orders of magnitude smaller than that at ω_0 and five orders smaller at $3\omega_0$. We thus neglect the influence of higher harmonic waves on the dynamics of waves at frequency ω_0 in this study.

b. Vertical-mode projections

Without background flow, the vertical modes defined in section 3c enable separation of the horizontal and vertical dependence of the flow and efficiently collapse the vertical coordinate. The choice of an adequate reference density profile is essential to this horizontal–vertical separation. A nonrepresentative $N(z)$ profile yields a complete basis, but modes are coupled linearly together such that the representation of the evolution of a true/intrinsic mode (i.e., defined with the actual stratification profile) requires, in general, to consider the evolution of several modes instead of just one. The term responsible for this coupling in the equations of motions is that associated with $\hat{w} \partial_z \bar{b}$ in (5) or equivalently $\hat{w}_m \bar{p}_l$ in (A5) and (A6). In other terms, a flow described by exactly one intrinsic-mode projects onto several of

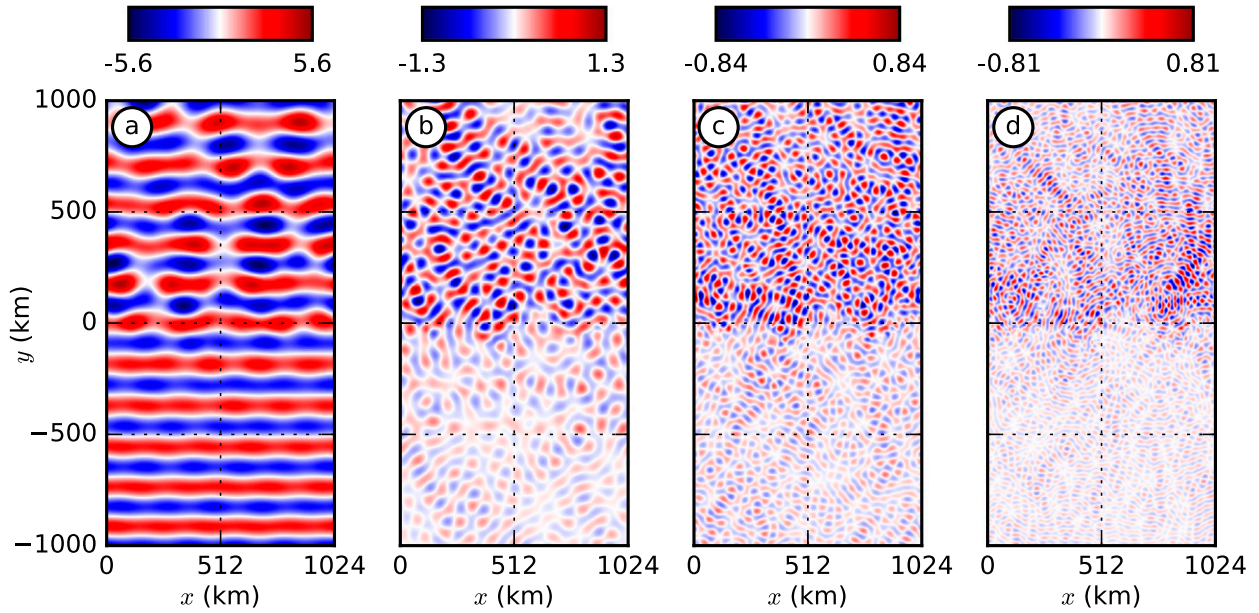


FIG. 5. Projected tidal frequency vertical velocity \hat{w}_n (mm s^{-1}) at $t = 3000$ days for (a)–(d) modes one through four. Each field is multiplied by the maximum of $|d/dz[\phi_n(z)]/N^2(z)|$, such that the maps represent the peak contribution to \hat{w} via (9).

the modes defined with a nonrepresentative stratification, misleadingly indicating that the flow is composed of multiple modes.

Thus, we would like to select $N(z)$ in a manner that preserves the intuitive modal interpretation as much as possible. However, the present experiment is stratified with north and south profiles and has a transition region in the domain center (see Fig. 1a); that is, it is not horizontally uniform. It is not obvious how to best choose $N(z)$ here; choosing the north profile is representative of the north part of the domain but not for the south part (and vice versa), and a domain-averaged profile would be approximate almost everywhere. To proceed we partition the domain into three zonal bands designated as the south region where $y \in [-1000, -500]$ km, the center region where $y \in [-500, 500]$ km, and the north region where $y \in [500, 1000]$ km. Horizontally averaging the slow density $\bar{\rho}$ over each partition gives three profiles, which we use in a piecewise constant fashion. Stitching together projections over each region forms complete fields. This choice has the advantage of using a representative profile in both the north and south regions, while compromising with an intermediate profile in the center.

Figure 5 shows horizontal maps of projected vertical velocity for modes one through four. We note that \hat{w}_n is proportional to the horizontal divergence via (19). The first mode shows a near-plane wave in the south part of the domain that becomes progressively distorted toward

the north. At mode two, a disorganized wave field forms with larger magnitudes in the north of the domain. Similar patterns appear at modes three and four at smaller amplitude. If we had used the north density profile in the south (and vice versa) then we would see patterns corresponding to a mode-one wavelength in the maps of modes two through four.

1) KINETIC ENERGY BREAKDOWN

We now assess the slow and fast fields in terms of energy at each mode. Table 2 lists the horizontal kinetic energy found at the barotropic and first four baroclinic modes taken at $t = 3000$ days. For the slow fields, we sum over the three analysis regions and find that the barotropic and first baroclinic mode each capture about half of the energy with a few percent spread over higher modes. The slow velocities are consistent with a red spectrum; the lowest modes dominate in terms of energy.

For the wave part, we assess the south and north regions separately. In the south region, the first baroclinic mode explains over 99.7% with the remainder found at modes two and above. Meanwhile in the north region, the first mode explains only 98.6% (a reduction of 1.1%), and the energy apportioned to modes two and above has risen. Barotropic waves are negligible in both regions. If the southern profile of stratification had been used in the northern part of the domain, the wave energy would have been more largely spread across modes (97.3% and 2.3% for mode one and two, respectively),

TABLE 2. Horizontal kinetic energy breakdown at $t = 3000$ days into vertical-mode contributions (%) for the quasigeostrophic part summed over the three regions and the wave part in the south and north regions.

Mode	Slow	Wave, S	Wave, N
0	51.491	0.000	0.000
1	45.524	99.787	98.603
2	1.895	0.131	0.991
3	0.406	0.056	0.316
4	0.250	0.015	0.064

indicating a stronger vertical scattering than there actually is and justifying the use of multiple reference profiles.

2) ENERGY FLUX DISTORTION

The wave field in the north part of the domain has been distorted after propagating through the quasigeostrophic turbulent field (Fig. 5). The interaction has introduced distortions that adjust propagation directions such that parts of the wave field do not propagate due north. Similarly at modes two through four we have a disorganized wave field that apparently emanates from the center region and propagates northward (southward) through the north (south) region.

To quantify these distortions, we first compute the temporal mean of the mode- n energy flux over the snapshots saved in $t = [2500, 3000]$ days and further take the spatial mean over the north and south regions to obtain a mean energy flux vector. We also compute the standard deviation over the same snapshots and same spatial area and normalize them by the magnitude of the mean energy flux, yielding a distortion metric we call d_n . The mean energy flux and distortion metric are reported in Table 3 for modes one through four.

The north component of the mean energy flux shows that mode-one energy flows to the north in both analysis regions. The net northward energy flux is reduced in the north, which may be explained by directional refraction in the horizontal that converts a portion of the meridional flux to zonal flux and/or due to the vertical mode scattering to higher modes. Meanwhile, the meridional energy flux at the higher modes shows that the net flux is north (south) in the north (south) region, which is consistent with the vertical scattering to higher modes of the mode-one incident wave occurring in the center of the domain.

The distortion metric at mode-one confirms that the wave field in the north region is more distorted than in the south. Variability of zonal energy flux rises from 0.08 in the south to 0.21 in the north. Variability of meridional energy fluxes rises from 0.04 in the south to 0.50 in the

TABLE 3. Mean energy flux and distortion metric computed over the snapshots taken in $t \in [2500, 3000]$ days.

n	Region	\overline{F}_n^y (W m^{-1})	d_n^x	d_n^y
1	North	2662.8	0.21	0.50
1	South	2878.6	0.08	0.04
2	North	14.0	0.62	1.08
2	South	-1.6	0.72	1.05
3	North	2.0	0.85	1.17
3	South	-0.4	0.58	1.05
4	North	0.4	0.64	1.12
4	South	-0.1	0.50	1.07

north, indicating that deviations are typically half the magnitude of the mean flux there. At modes two through four, we see that the wave is similarly distorted in the north as compared to the south. Variabilities of both zonal and meridional energy fluxes are stronger than seen at mode one, reaching 0.85 and 1.17, respectively.

c. Projected equation balances

Owing to the complexity of the interaction terms in the general case, the dynamics of the internal wave propagation are inspected through the scope of associated momentum and pressure equations [(17) and (18)]. These equations are indeed the ones that would be time stepped by a simplified predictive model of low-mode propagation. An alternative would have been to derive and analyze a wave equation that includes interactions with the background flow, but this would be conceptually more complex. To construct horizontal maps of terms in these momentum and pressure equations, we project separately for the north, center, and south $N(z)$ profiles and then stitch the regions together to obtain horizontally complete fields. Cosine fits form the linear terms except for the time derivatives where we use $\partial_t \hat{v}_n^{\text{cos}} = i\omega \hat{v}_n^{\text{sin}}$ and $\partial_t \hat{p}_n^{\text{cos}} = i\omega \hat{p}_n^{\text{sin}}$. The interaction terms use the slow averages and cosine fits. We truncate the sums at $M = L = 8$, which is enough to capture the energetic modes (see Table 2).

Figure 6 illustrates the tidal frequency balance for the meridional momentum equation at mode-one taken at $t = 3000$ days. Maps of the linear terms appear in Figs. 6a and 6b, the sum of the linear terms is in Fig. 6c, and the interaction term is in Fig. 6d. The linear terms form the dominant balance, the sum of which balances with the interaction term. The residual between linear and interaction terms (not shown) is one order of magnitude smaller than the interaction term of Fig. 6d. The interaction term shows patches alternating in sign that are confined to the middle portion of the domain where the quasigeostrophic field is present. The ratio of the root-mean-square (rms) momentum interaction term to rms momentum time derivative term is 0.021, which is

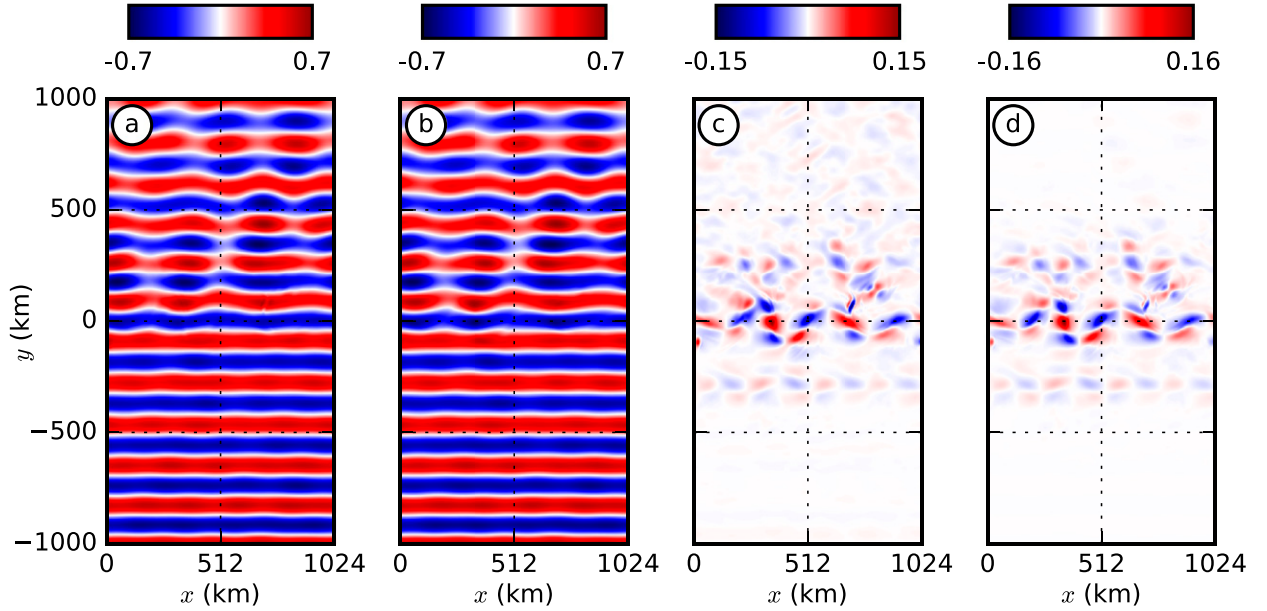


FIG. 6. Maps of the meridional momentum equation [(17)] for mode one at $t = 3000$ days, showing (a) the time derivative plus Coriolis terms $\partial_t \tilde{v}_1 + f \tilde{u}_1$, (b) the pressure gradient $-\partial_y \tilde{p}_1$, (c) the linear term balance $\partial_t \tilde{v}_1 + f \tilde{u}_1 + \partial_y \tilde{p}_1$, and (d) the interaction term I_1^p . Each term is nondimensionalized by \tilde{v}_1 , the rms of the time derivative term taken over the center region ($\tilde{v}_1 = 2.64 \times 10^{-6} \text{ m s}^{-2}$).

about a factor of 1.6 larger than its expected value from the scaling analysis: $R\mu/\bar{\omega} \sim 0.013$ using (R, μ) associated with eddies and meanders. Contributions of the first three terms on the right-hand side of (A2) are found to be of comparable amplitude, which is consistent with nondimensional scalings (see appendix B with μ only slightly larger than unity for eddies). Consistent with these scalings, the fourth term is, on the other hand, smaller by about a Rossby number factor. This fourth term corresponds to the vertical advection of the wave momentum by the slow vertical flow and is small due to the weakness of quasigeostrophic vertical velocity.

Figure 7 shows analogous maps for the first-mode pressure equation with the linear terms in Figs. 7a and 7b, their sum in Fig. 7c, and the interaction term in Fig. 7d. As in the momentum equation, the linear terms form the dominant balance and the sum of the linear terms balances with the interaction term. Here, the interaction term shows an apparent discontinuity at the boundaries separating the three analysis regions (along $y = \pm 500$ km). This is a consequence of using piecewise constant $N(z)$ profiles for vertical-mode projection where the background stratification horizontally varies.

Separating the slow pressure into zonal anomaly (ZA) and ZM parts via (A3) divides the interaction term into two parts, as in (A4), and they are shown in Fig. 8. The rms of the zonal mean part $I_1^{p,ZM}$ is roughly 4 times that of the zonal anomaly part $I_1^{p,ZA}$, and the zonal anomaly part shows patterns reminiscent of the interaction term

in the momentum equation. The ratio of the rms pressure interaction term to the rms pressure time derivative is 0.15, which is comparable to the expected value from the scaling analysis: $R\mu^2/(\bar{\omega}^2 - 1) \sim 0.11$ with (R, μ) associated with the large-scale change of stratification. Of the four terms on the right-hand side of (A5) and (A6), the second term, that is, the vertical advection of the slow stratification by the wave, dominates. This dominance is expected from the μ^2 scaling of this term (appendix B) when $\mu > 1$, as is the case for the large-scale meridional change of stratification.

d. Interaction term approximations

Some knowledge of the slow quasigeostrophic circulation would be necessary in order to predict the evolution of low-mode internal waves. This section is an attempt at quantifying the required temporal, horizontal, and vertical resolution information in order to correctly carry out such predictions. For that purpose, we approximate the interaction terms by computing them with a quasigeostrophic field of degraded resolution and compare them with their actual values via the skill metric

$$S = 1 - \frac{\int_A (I - I^*)^2 dA}{\int_A I^2 dA}, \tag{23}$$

where I^* is the approximation to I , and area A is the zonal band bounded by $y = \pm 500$ km. Values of zero and one

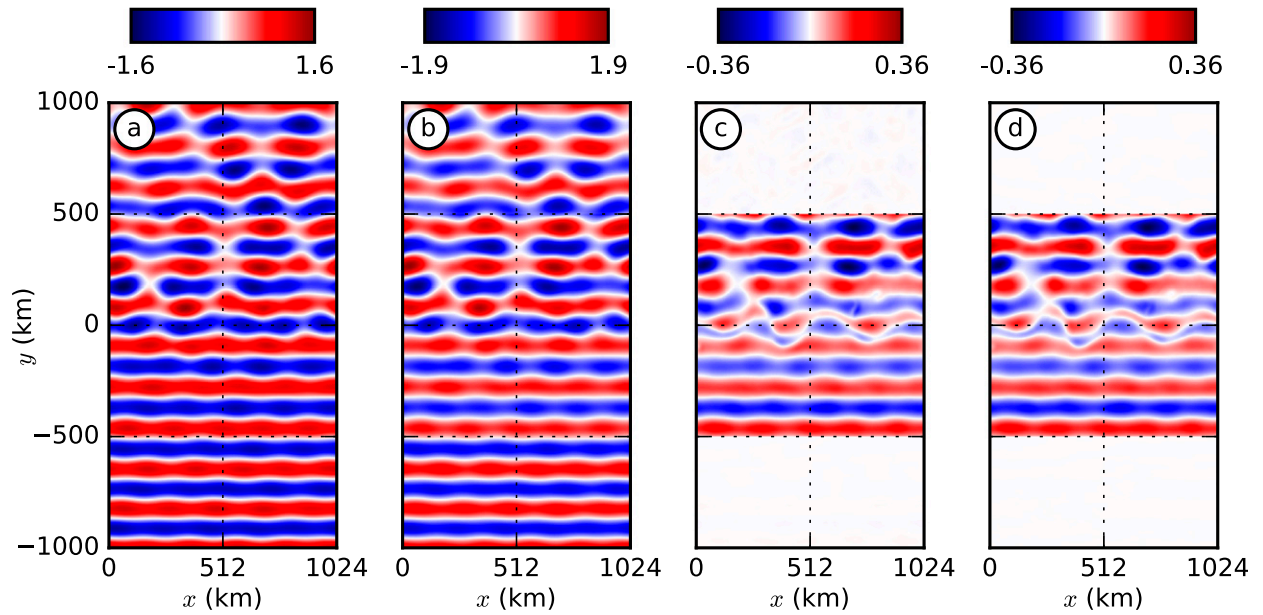


FIG. 7. Maps of the pressure equation [(18)] for mode one at $t = 3000$ days, showing (a) the time derivative term $\partial_t \hat{p}_1$, (b) the horizontal divergence term $-c_1^2 \nabla_h \cdot \hat{\mathbf{u}}_{n,1}$, (c) the linear term balance $\partial_t \hat{p}_1 + c_1^2 \nabla_h \cdot \hat{\mathbf{u}}_{n,1}$, and (d) the interaction term I_1^p . Each term is non-dimensionalized by \hat{p}_1 , the rms of the time derivative term taken over the center region ($\hat{p}_1 = 1.14 \times 10^{-5} \text{ m}^2 \text{ s}^{-3}$).

indicate zero and perfect skill, respectively. Note that it is a priori unclear how an error in the interaction term translates into an error in a wave field prediction, but the proper estimation of these terms is considered at least a necessary condition for such prediction.

The Argo network and satellite estimates of sea level are the main two sources of information about the ocean circulation (Le Traon 2013) and their spatiotemporal sampling rates provide a useful perspective for the numbers coming next. The mean Argo float density is one float per $300 \text{ km} \times 300 \text{ km}$ box and vertical profiles of temperature and salinity are taken every 10 days. The merging of multiple altimeter datasets resolves wavelengths longer than 200 km with a temporal resolution of about 20 days. Note that the inference of the mesoscale/submesoscale ocean circulation from combined altimetric and Argo data remains at present an outstanding challenge (Ferrari and Wunsch 2010; Le Traon 2013; Klein et al. 2015).

1) HORIZONTAL AND TEMPORAL RESOLUTION

To degrade the horizontal resolution, we convolve the slow fields with the boxcar filter

$$b(x, y) = \begin{cases} \frac{1}{q^2} & \text{if } |x| < q/2 \text{ and } |y| < q/2, \\ 0 & \text{otherwise,} \end{cases} \quad (24)$$

where q is the filter width, and compute the interaction terms using the degraded slow fields. Figure 9a shows

the skill [(23)] in approximating the interaction terms for increasing values of q . For I_1^p in the meridional momentum equation, the skill exceeds 0.9 for filters up to 74 km. For the pressure equation, the ZM part is, as expected, largely unaffected by the smoothing with skill exceeding 0.99 for filters up to 300 km wide. Meanwhile

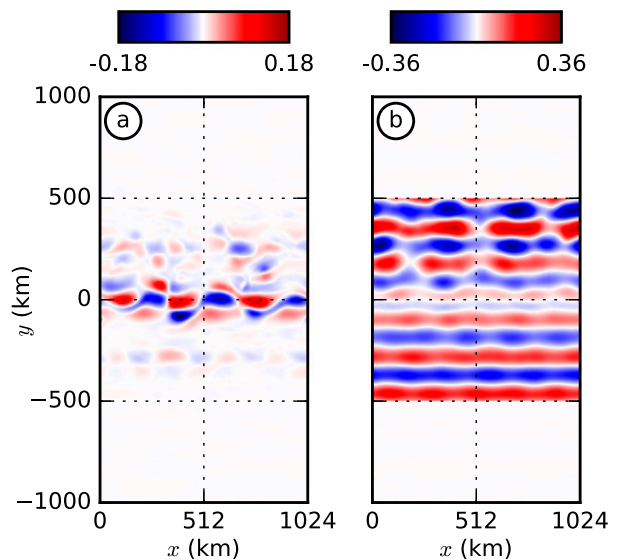


FIG. 8. Figure 7d separated into two parts, showing (a) the contribution from the variations in slow pressure due to eddies and meanders $I_1^{p,ZA}$ and (b) the contribution from the across-jet variation in slow pressure $I_1^{p,ZM}$.

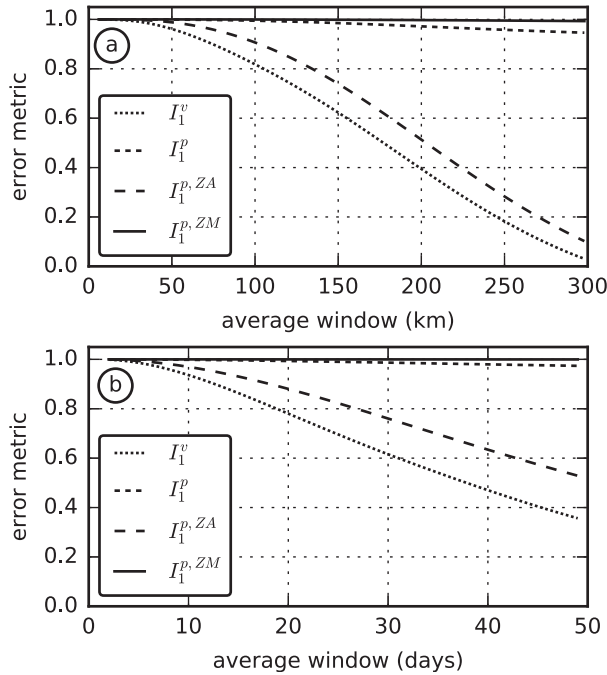


FIG. 9. Skill in approximating the interaction terms constructed with degraded quasigeostrophic fields. (a) A centered boxcar filter to reduce horizontal resolution and (b) a sliding average filter to reduce temporal resolution.

the ZA part degrades to a skill level of 0.9 with filters of 102-km width.

For temporal resolution, we employ the sliding average filter (1) and use the daily model outputs saved between $t = 3000$ and 3050 days. Figure 9b shows the corresponding skill curves. Approximations for I_1^v at $t = 3050$ days exceed 0.9 with 12 days of averaging, while approximations for $I_1^{p,ZA}$ exceed 0.9 after averaging for 18 days. The zonal mean part $I_1^{p,ZM}$ skill remains above 0.99 even with 50 days of averaging.

These results thus suggest that while the resolution of the Argo network and altimetric data should be sufficient to capture the effect of the large-scale meridional change of stratification on the mode-one propagation, this may not be the case for meanders and eddies such as those that develop in the present setting. Upcoming missions such as SWOT with its wide-swath capability could significantly improve upon this situation, provided the extrapolation of sea level data into information about the vertical structure of the flow can be achieved (Klein et al. 2015).

2) VERTICAL RESOLUTION

The vertical coupling in the modal equations is represented in the interaction terms through sums that collect the influence between each wave mode and each

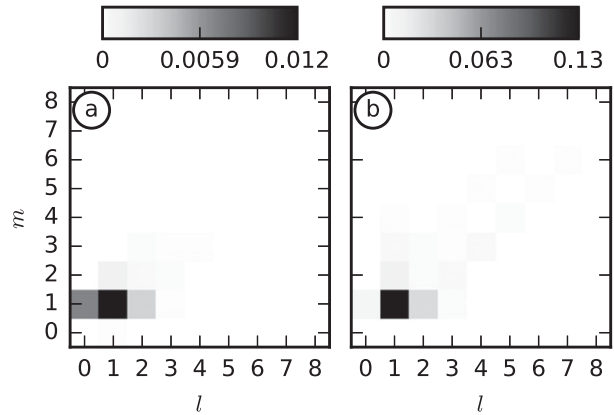


FIG. 10. Total interaction terms broken into interactions between each wave mode m and quasigeostrophic mode l at $t = 3000$ days: (a) I_1^v and (b) I_1^p . Each marker represents the rms value taken over the center region and nondimensionalized by \bar{v}_1 and \bar{p}_1 as in Figs. 6 and 7.

slow mode. Figure 10 shows the magnitude (rms over the center region) of each pair of interacting modes for I_1^v and I_1^p . The figure reveals that contributions from a few low modes dominate the sums. Specifically, wave mode $m = 1$ and slow mode $l = 1$ dominate both interaction terms and wave mode $m = 1$ and slow modes $l = 0, 2$ are the next most important. That these modes are largest in magnitude is readily reconciled with the kinetic energy breakdown of Table 2, which showed wave mode $m = 1$ and slow modes $l = 0, 1$ contain most of the energy.

Having identified the most important contributions to the interaction terms, we consider approximating the full interaction term with reconstructions built from including just a few m, l pairs. The result of this exercise shows that the skill in estimating the momentum interaction term starts at 0.79 when mode $(m = 1, l = 1)$ is considered alone and increases to 0.96 and 0.99 when modes $(1, 0)$ and $(1, 2)$ are added successively. On the other hand, the skill in estimating the pressure interaction term starts at 0.96 with mode $(1, 1)$ alone and increases to 0.996 when $(1, 2)$ is included. These results are consistent with the observed weak vertical scattering of the internal wave (Table 2). They also suggest that, based on a 0.9 skill threshold, keeping track of a single wave mode along with the knowledge of the slow circulation's lowest two modes may be sufficient in order to estimate the evolution of the internal tide in a configuration comparable to the present one.

e. Mode-two forcing

We conducted a second simulation forced with a mode-two tide by resuming the spunup quasigeostrophic

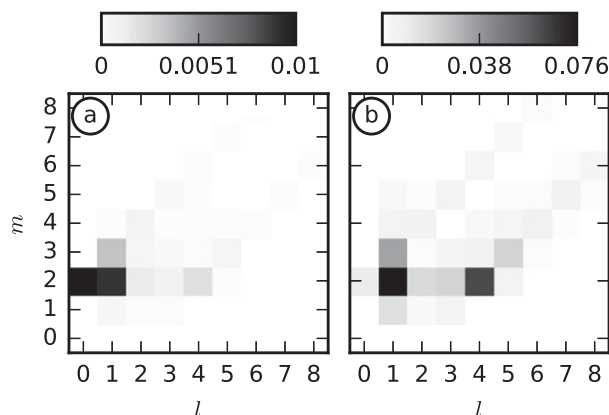


FIG. 11. As in Fig. 10, but with mode-two forcing: (a) I_2^l and (b) I_2^m .

field from $t = 2000$ days. The wave horizontal kinetic energy breakdown shows that the south region contains 99% mode two and 0.7% mode three, while the north contains 92% mode-two energy and 6.3% mode-three energy. The reduction of mode-two fraction suggests that this internal wave is scattered vertically more significantly than the mode-one wave. Normalized variabilities of mode-two zonal and meridional energy fluxes rise from 0.11 and 0.05 in the south to 0.48 and 0.96 in the north, respectively. These values are roughly twice those found in the mode-one forced case, indicating that mode-two waves are distorted more strongly than mode-one waves. This is consistent with prior research that found higher-mode internal tides are more strongly distorted by meso-scale circulation (Rainville and Pinkel 2006; Zaron and Egbert 2014).

Degradation of the slow field's resolution via spatial and temporal filtering reveals that skill remained above 0.9 for spatial filters up to 74 km (same as mode-one forced case) and that sensitivity to temporal averaging increased with skill dropping to 0.9 with 8 days of averaging. Prediction of mode-two internal waves thus requires marginally more temporal accuracy than for mode one.

Interaction terms are then decomposed into modal contributions as done for mode one (Fig. 11). Compared to the mode-one case, there is a larger spread of the modes that build up these terms. Based on a 0.9 skill threshold, estimations of the momentum interactions require not only to account for interactions between wave mode two and the lowest two slow modes, but also for that between wave mode three and slow mode one. This contribution from a different wave mode is attributed to the more important vertical scattering of the mode-two internal wave

compared to the mode-one case. Estimation of the pressure interaction terms requires keeping track of the wave mode two and up to the fourth slow mode. A more detailed knowledge of the slow-flow vertical structure is required in order to estimate the interaction of the mode-two wave with this slow-flow compared to the mode-one case. Note finally that the diagonals defined by $n = \pm m + l$ faintly appear in Fig. 11, which points toward the natural coupling that exists between these triads of vertical modes (Fu and Flierl 1980).

f. Stronger turbulence

We also conducted a third simulation where we strengthened the slow turbulence by increasing the north–south density contrast. The slow kinetic energy level is 4 times higher than the base case. Slow horizontal kinetic energy decomposes into 67% and 30% at the barotropic and first mode, respectively, with the remainder at modes two and above. For wave horizontal kinetic energy, mode one drops from 98% in the south to 95% in the north, suggesting that scattering to higher modes amounts to 3%, which is slightly higher than for the base case. The wave propagation is more strongly affected by the slow circulation, which is clearly visible on projections of the fast fields (not shown). Normalized variabilities of zonal and meridional energy fluxes rises from 0.11 and 0.05 in the south to 0.58 and 1.04, respectively, in the north. The same metrics for modes two through four follow those from the nominal turbulence case.

Spatial filtering revealed that skill remained above 0.9 for filters up to 62 km, a modest reduction as compared to the nominal turbulence case, while temporal averaging reduced the skill to 0.9 with 8 days of averaging. This modest decrease is concomitant with a decrease in the eddy time scale ($T_g \sim 1/f_0R$) associated with an increased Rossby number and suggests that more accurate temporal resolution may be required in order to predict the evolution of the internal wave in a stronger turbulent eddy field. An interaction term breakdown produces a plot comparable to Fig. 10 and is not shown. As in the base case, tracking the forced mode-one wave along with the knowledge of the lowest two modes in the slow circulation is sufficient to estimate interaction terms above a 0.9 skill threshold.

g. Scaling analysis validation

In this section, we evaluate the performance of the scaling analysis. We do this by estimating the nondimensional parameters from the model outputs and comparing the expected interaction term scaling

TABLE 4. Range of values estimated for the velocity/length scales and nondimensional parameters for both the zonal anomalies and means.

Turbulence forced wave	Nominal mode one	Nominal mode two	Strong mode one
Zonal anomalies			
U_g (cm s ⁻¹)	4.5–9.1	5.0–9.1	8.7–29
L_g (km)	25–53	29–53	37–68
R	0.014–0.019	0.014–0.018	0.019–0.046
μ	0.88–1.9	2.2–4.0	1.4–2.6
$R\mu$	0.015–0.031	0.036–0.066	0.032–0.11
$R\mu^2$	0.014–0.054	0.081–0.25	0.048–0.29
Zonal means			
U_g (cm s ⁻¹)	2.9–4.5	3.1–4.5	4.6–17
L_g (km)	190–280	190–290	190–320
R	0.0010–0.0023	0.0010–0.0023	0.0016–0.0086
μ	6.7–9.7	14–21	7.4–12
$R\mu$	0.0099–0.015	0.022–0.033	0.017–0.064
$R\mu^2$	0.094–0.11	0.47–0.51	0.17–0.49

with that obtained by computing the interaction terms directly.

For each interaction-phase model output, we separate the slow flow into contributions from eddies and jet meanders (by extracting zonal anomalies) and those from the large-scale meridional change of stratification (by extracting zonal means). We then estimate typical scales by computing the root-mean-square speed (for U_g) and pressure (for L_g via the scaling for \bar{p}_l) over the zonal band bounded by $y = \pm 500$ km. The dispersion relation provides the internal tide wavelength L_w . The range for each of these values and the corresponding nondimensional parameters are summarized in Table 4. The upper (lower) part of the table reports on the zonal anomalies (means). In Fig. 12, we plot the interaction term magnitude (computed as the root-mean-square over the same zonal band) against its expected scaling, where each marker represents one model output.

For the momentum equation (Fig. 12a), the interaction term scales as expected, although the performance is better for the mode-two wave than for the mode-one wave. For the pressure equation, the interaction term due to zonal anomalies (Fig. 12b) scales as expected, with the exception of a few early time [$t \in (2000, 2200)$ days] outputs from the strong turbulence case. Last, the interaction term due to zonal means (Fig. 12c) also scales as expected within a constant factor, with similar mismatches for the first few outputs. The remaining markers are tightly clustered, and this is expected because the large-scale change in stratification varies little during the interaction phase.

While the scaling performs well, we note that mismatches may be due to (i) selecting a single term for the scaling, where it is only marginally larger than others

that are neglected [see (B1) and (B2)] and (ii) characterizing the slow flow with a single Rossby number. A more detailed scaling analysis might include both a barotropic and first-mode Rossby number.

5. Conclusions and discussion

This work investigated interactions between a plane low-mode internal wave and a slowly evolving turbulent jet. The underlying goal is to assess the feasibility of predicting the propagation of internal tides with a simplified dynamical model. Such a model may facilitate the disentanglement of internal tide and slower quasigeostrophic motions from upcoming high-resolution satellite observations of sea level (SWOT).

Linearization of the equations of motions (momentum, pressure) around the slow circulation combined with a projection onto vertical modes provided a dynamical framework in order to represent the evolution of the wave as it propagates through the slow turbulence. A scaling analysis of these equations was performed in order to highlight the dependence of interaction terms on the slow-flow Rossby number and on the ratio of the slow-flow length scale to that of the wave. Each term involved in the wave momentum and pressure evolution equations was then diagnosed from the numerical simulation outputs. In accordance with the scaling analysis, eddies and jet meanders were found to dominate the wave momentum evolution, while the large-scale meridional change of stratification was found to control the pressure evolution. The scaling analysis was validated against each model output and found to agree well.

The estimation of these interaction terms requires an estimate of the slow circulation, which will be

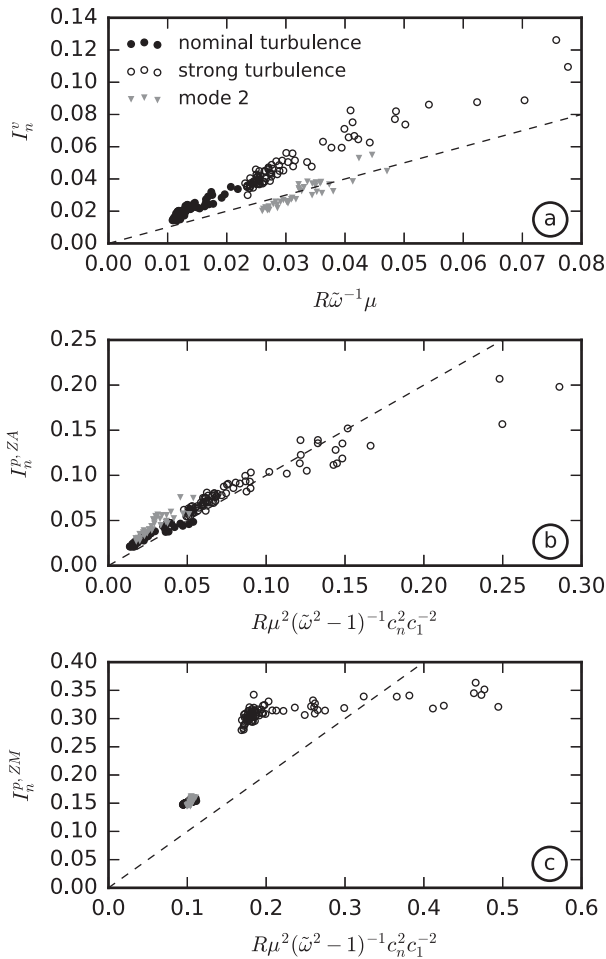


FIG. 12. Scatterplot showing the scaling estimates and the rms interaction term (a) I_n^v , (b) $I_n^{p,ZA}$, and (c) $I_n^{p,ZM}$. The dashed line shows the 1:1 line.

approximate in practice. The impact of a degradation of our knowledge of the slow circulation upon the estimation of interaction terms was thus quantified. A horizontal spatial resolution of about 70 km and a temporal resolution of about 10 days were found to be sufficient in order to correctly quantify these interactions. Waves with higher vertical modes and stronger slow turbulence require marginally more temporal resolution. These results suggest that the present-day observation system (Argo, altimetry) may not provide estimates of the mesoscale circulation with sufficient spatial resolution in order to estimate the impact of the slow-flow circulation on low-mode internal waves and tides. The upcoming wide-swath, high-resolution altimetric mission SWOT, on the other hand, may significantly improve upon this situation, provided that the ocean circulation (not only at the surface but also at depth) may be inferred from the SWOT sea level.

Because the interaction between the wave and the slow flow may involve the coupling between any vertical modes, we also addressed the sensitivity of interaction term estimates to the number of modes included. For an incident mode-one internal wave, the vertical scattering of the wave is weak enough such that keeping track of this mode alone is sufficient in order to predict its evolution. This is not the case for a mode-two incident wave whose vertical scattering is more important and for which the combined interaction of wave mode three with the slow flow becomes significant. Some vertical resolution of the slow field is required in order to correctly estimate the interaction between the wave and the slow flow. For a mode-one incident wave, knowledge of the barotropic mode and the first baroclinic mode is sufficient. For a mode two on the other hand, knowledge of the fourth mode may be required, which may be a strong constraint in an operational context. Bathymetric variations will induce vertical scattering, which we anticipate will impose stronger constraints on the vertical resolution required to predict the evolution of the internal tide, but this was not addressed here.

This work shows as well that the vertical-mode representation does not come without challenge. The significant signature on the pressure interaction associated with the large-scale change of stratification is tightly related to the necessary choice of a reference profile that may not be adequate over the whole domain considered. We chose here to divide the domain into three parts and used three different profiles in order to compute diagnostics. The time stepping to calculate internal tide evolution with such a decomposition will require the application of continuity conditions at the boundaries between each subdomain whose details were not discussed here. An alternative would be to account within the wave equations of motions for the continuous variations of the background stratification. Such approach has been considered by Griffiths and Grimshaw (2007) and Kelly et al. (2013) in order to deal with bathymetric variations. If such approaches do not perform well, an alternative to the vertical-mode projections may be needed. Resorting to the vertical physical dimension may be an option that will be more expensive computationally but may facilitate the dynamical interpretation of internal wave-balanced flow interactions.

A limitation of the dynamical framework used here is that we ignore the feedback of the internal tide on balanced motions. We have also ignored the production of and interactions with motions at harmonic

frequencies. Xie and Vanneste (2015) and Wagner and Young (2016) showed that both are important for the long-term evolution of near-inertial motions. Similar results still await for internal tides, but, if established, a significant improvement upon the dynamical framework employed here may be one that represents the evolution of three components (internal tide, internal tide harmonics, and balanced motions) as done in Wagner and Young (2016) for near-inertial waves. Interestingly, the assimilation of observations into such framework may provide a natural way to estimate the ocean circulation and disentangle each process simultaneously.

Acknowledgments. The authors acknowledge support from CNES’s SWOT mission and from the Agence Nationale pour la Recherche (ANR-10-LABX-19-01, LabexMER). We acknowledge that the results of this research have been achieved using the PRACE Research Infrastructure resource Fermi based in Italy at CINECA (through allocation 2014102346) and using HPC resources from GENCI (through Grant t2016017515). Postdoctoral fellowship support for M. Dunphy was provided by IFREMER.

APPENDIX A

Interaction Terms

The interaction terms in the projected zonal and meridional momentum equations [(16) and (17)] at mode n are

$$I_n^u(\hat{\mathbf{u}}, \bar{\mathbf{u}}) = - \sum_{m=0}^M \sum_{l=0}^L [\alpha_{n,m,l}(\hat{\mathbf{u}}_{h,m} \cdot \nabla_h) \bar{u}_l + \beta_{n,m,l} \hat{w}_m \bar{u}_l] + [\alpha_{n,m,l}(\nabla_h \hat{u}_m) \cdot \bar{\mathbf{u}}_{h,l} + \beta_{n,m,l} \hat{u}_m \bar{w}_l], \quad \text{and} \quad (\text{A1})$$

$$I_n^v(\hat{\mathbf{u}}, \bar{\mathbf{u}}) = - \sum_{m=0}^M \sum_{l=0}^L [\alpha_{n,m,l}(\hat{\mathbf{u}}_{h,m} \cdot \nabla_h) \bar{v}_l + \beta_{n,m,l} \hat{w}_m \bar{v}_l] + [\alpha_{n,m,l}(\nabla_h \hat{v}_m) \cdot \bar{\mathbf{u}}_{h,l} + \beta_{n,m,l} \hat{v}_m \bar{w}_l], \quad (\text{A2})$$

where the first set of brackets encloses the refractive terms (advection of the slow flow by the waves), and the second encloses the Doppler shift terms (advection of the waves by the slow flow). Each of these two terms is decomposed into two parts associated with horizontal and vertical advection, respectively. The double summations collect the interaction between wave mode m and slow-flow mode l . Meanwhile, we

divide the slow pressure into a ZA part and a ZM part,

$$\bar{p}_l = \bar{p}_l^{\text{ZA}}(x, y) + \bar{p}_l^{\text{ZM}}(y), \quad (\text{A3})$$

which separates the interaction term in the projected pressure equation [(18)] at mode n into two corresponding parts:

$$I_n^p(\hat{\mathbf{u}}, \bar{\mathbf{u}}, \hat{p}, \bar{p}) = I_n^{p,\text{ZA}}(\hat{\mathbf{u}}, \bar{\mathbf{u}}, \hat{p}, \bar{p}^{\text{ZA}}) + I_n^{p,\text{ZM}}(\hat{\mathbf{u}}, \bar{p}^{\text{ZM}}), \quad (\text{A4})$$

where

$$I_n^{p,\text{ZA}} = - \sum_{m=0}^M \sum_{l=0}^L [\gamma_{n,m,l}(\hat{\mathbf{u}}_{h,m} \cdot \nabla_h) \bar{p}_l^{\text{ZA}} + \delta_{n,m,l} \hat{w}_m \bar{p}_l^{\text{ZA}}] + [\gamma_{n,m,l}(\nabla_h \hat{p}_m) \cdot \bar{\mathbf{u}}_{h,l} + \delta_{n,m,l} \hat{p}_m \bar{w}_l], \quad \text{and} \quad (\text{A5})$$

$$I_n^{p,\text{ZM}} = - \sum_{m=0}^M \sum_{l=0}^L [\gamma_{n,m,l}(\hat{\mathbf{u}}_{h,m} \cdot \nabla_h) \bar{p}_l^{\text{ZM}} + \delta_{n,m,l} \hat{w}_m \bar{p}_l^{\text{ZM}}], \quad (\text{A6})$$

and where the brackets separate the terms as in the momentum equation. Last, the vertical mode coupling coefficients are

$$\alpha_{n,m,l} = \langle \phi_n \phi_m \phi_l \rangle, \quad (\text{A7})$$

$$\beta_{n,m,l} = \langle \phi_n \phi'_m \phi'_l / N^2 \rangle, \quad (\text{A8})$$

$$\gamma_{n,m,l} = \langle \phi'_n \phi'_m \phi_l c_n^2 / N^2 \rangle, \quad \text{and} \quad (\text{A9})$$

$$\delta_{n,m,l} = \langle \phi'_n \phi''_m \phi'_l c_n^2 / N^4 \rangle, \quad (\text{A10})$$

where $\langle \cdot \rangle$ denotes the inner product [(13)], and the prime notation denotes differentiation with respect to z .

APPENDIX B

Interaction Term Scaling

To scale the interaction terms, we retain only the most important terms in the double summations. For our present cases, the incident wave mode dominates the wave terms ($n = m = 1$ or 2), and the barotropic and first mode dominate the slow flow ($l = 0$ and $l = 1$). Over these values of n and l , the coupling coefficients scale as

$$\alpha_{n,n,l} \sim 1, \quad \beta_{n,n,l} \sim \sigma_l / c_n c_l,$$

$$\gamma_{n,n,l} \sim 1, \quad \delta_{n,n,l} \sim \sigma_l / c_n c_l,$$

where $\sigma_0 \sim c_1 / c_0 \ll 1$ and $\sigma_l = 1$ for $l \geq 1$. Approximate scalings for the interaction terms follow:

$$I_n^{u,v} \sim R\tilde{\omega}^{-1} \underbrace{\left[\overbrace{(1) + (0)}^{\text{refractive}} + \overbrace{(\mu) + \left(\frac{c_1}{c_n} R\right)}^{\text{Doppler}} \right]}_{l=0} + R\tilde{\omega}^{-1} \underbrace{\left[\overbrace{(1) + \left(\frac{c_n}{c_1} \mu\right)}^{\text{refractive}} + \overbrace{(\mu) + \left(\frac{c_1}{c_n} R\right)}^{\text{Doppler}} \right]}_{l=1}, \quad \text{and} \quad (\text{B1})$$

$$I_n^p \sim \underbrace{\frac{R\mu}{\tilde{\omega}^2 - 1} \left[\overbrace{(0) + (0)}^{\text{refractive}} \right] + R\tilde{\omega}^{-1} \left[\overbrace{(\mu) + \left(\frac{c_1}{c_n} R\right)}^{\text{Doppler}} \right]}_{l=0} + \underbrace{\frac{R\mu}{\tilde{\omega}^2 - 1} \left[\overbrace{\left(\frac{c_n}{c_1}\right) + \left(\mu \frac{c_n^2}{c_1^2}\right)}^{\text{refractive}} \right] + R\tilde{\omega}^{-1} \left[\overbrace{(\mu) + \left(\frac{c_1}{c_n} R\right)}^{\text{Doppler}} \right]}_{l=1}, \quad (\text{B2})$$

where we have neglected terms proportional to σ_0 . The ratio c_1/c_n and the nondimensional frequency are order one (as $n = 1$ or 2) in the present work but are retained in order to keep a sensitivity to the choice of the incident wave mode number and frequency, respectively. All terms, except those related to the vertical advection by the slow flow, are proportional to the Rossby number. The vertical advection by the slow flow is proportional to the square of the Rossby number and thus remains small compared to others. Differences in the scaling of leading-order terms arise from their dependence on the length-scale ratio μ . This length-scale ratio appears in horizontal advective terms (third term in each line) and reflects the dominance of advective terms when the slow flow has large scales compared to the internal tide ($\mu \gg 1$ and $l = 0$ when WKB approaches are valid). The length-scale ratio also appears in the refraction term associated with vertical advection by the wave (second term), which is explained by the absence of vertical-scale separation between the wave and the slow flow. The length-scale ratio scales all refractive terms in the pressure interaction terms (first and second terms), which arises from the geostrophic pressure scaling (section 3e). At small Rossby number, the overall terms scale with

$$I_n^{u,v} \sim R\tilde{\omega}^{-1} \max(1, \mu), \quad \text{and} \quad (\text{B3})$$

$$I_n^p \sim R\mu \max\left(\tilde{\omega}^{-1}, \frac{1}{\tilde{\omega}^2 - 1} \frac{c_n}{c_1}, \frac{\mu}{\tilde{\omega}^2 - 1} \frac{c_n^2}{c_1^2}\right), \quad (\text{B4})$$

revealing the importance of the length-scale ratio μ . The horizontal velocity interaction term scales with μ when $\mu > 1$, and the pressure interaction term scales with μ^2 when $\mu > c_1/c_n$. Setting $n = 1$ yields the right-hand sides of (21) and (22).

REFERENCES

- Arbic, B. K., A. J. Wallcraft, and E. J. Metzger, 2010: Concurrent simulation of the eddying general circulation and tides in a global ocean model. *Ocean Modell.*, **32**, 175–187, doi:10.1016/j.oceanmod.2010.01.007.
- , F. Lyard, A. Ponte, R. Ray, J. G. Richman, J. F. Shriver, E. Zaron, and Z. Zhao, 2015: Tides and the SWOT mission: Transition from science definition team to science team. Tech. Rep. CNES-NASA, 8 pp.
- Bühler, O., 2014: *Waves and Mean Flows*. 2nd ed. Cambridge University Press, 360 pp.
- , and M. E. McIntyre, 2005: Wave capture and wave-vortex duality. *J. Fluid Mech.*, **534**, 67–95, doi:10.1017/S0022112005004374.
- Danioux, E., J. Vanneste, and O. Bühler, 2015: On the concentration of near-inertial waves in anticyclones. *J. Fluid Mech.*, **773**, R2, doi:10.1017/jfm.2015.252.
- Dufau, C., M. Orszynowicz, G. Dibarboure, R. Morrow, and P.-Y. Le Traon, 2016: Mesoscale resolution capability of altimetry: Present and future. *J. Geophys. Res. Oceans*, **121**, 4910–4927, doi:10.1002/2015JC010904.
- Dunphy, M., and K. G. Lamb, 2014: Focusing and vertical mode scattering of the first mode internal tide by mesoscale eddy interaction. *J. Geophys. Res. Oceans*, **119**, 523–536, doi:10.1002/2013JC009293.
- Ferrari, R., and C. Wunsch, 2010: The distribution of eddy kinetic and potential energies in the global ocean. *Tellus*, **62A**, 92–108, doi:10.3402/tellusa.v62i2.15680.
- Fu, L.-L., and G. R. Flierl, 1980: Nonlinear energy and entropy transfers in a realistically stratified ocean. *Dyn. Atmos. Oceans*, **4**, 219–246, doi:10.1016/0377-0265(80)90029-9.
- Garrett, C., and E. Kunze, 2007: Internal tide generation in the deep ocean. *Annu. Rev. Fluid Mech.*, **39**, 57–87, doi:10.1146/annurev.fluid.39.050905.110227.
- Gill, A. E., 1982: *Atmosphere–Ocean Dynamics*. Academic Press, 662 pp.
- Griffiths, S. D., and R. H. Grimshaw, 2007: Internal tide generation at the continental shelf modeled using a modal decomposition: Two-dimensional results. *J. Phys. Oceanogr.*, **37**, 428–451, doi:10.1175/JPO3068.1.
- Kelly, S. M., N. L. Jones, and J. D. Nash, 2013: A coupled model for Laplace’s tidal equations in a fluid with one horizontal dimension and variable depth. *J. Phys. Oceanogr.*, **43**, 1780–1797, doi:10.1175/JPO-D-12-0147.1.
- Kerry, C. G., B. S. Powell, and G. S. Carter, 2014: The impact of subtidal circulation on internal-tide-induced mixing in the Philippine Sea. *J. Phys. Oceanogr.*, **44**, 3209–3224, doi:10.1175/JPO-D-13-0249.1.
- Klein, P., B. L. Hua, G. Lapeyre, X. Capet, S. L. Gentil, and H. Sasaki, 2008: Upper ocean turbulence from high-resolution 3D simulations. *J. Phys. Oceanogr.*, **38**, 1748–1762, doi:10.1175/2007JPO3773.1.

- , and Coauthors, 2015: Mesoscale/submesoscale dynamics in the upper ocean. Tech. Rep. CNES-NASA, 13 pp.
- Le Traon, P. Y., 2013: From satellite altimetry to Argo and operational oceanography: Three revolutions in oceanography. *Ocean Sci.*, **9**, 901–915, doi:10.5194/os-9-901-2013.
- Plougonven, R., and C. Snyder, 2005: Gravity waves excited by jets: Propagation versus generation. *Geophys. Res. Lett.*, **32**, L18802, doi:10.1029/2005GL023730.
- Polzin, K. L., 2010: Mesoscale eddy-internal wave coupling. Part II: Energetics and results from PolyMode. *J. Phys. Oceanogr.*, **40**, 789–801, doi:10.1175/2009JPO4039.1.
- Rainville, L., and R. Pinkel, 2006: Propagation of low-mode internal waves through the ocean. *J. Phys. Oceanogr.*, **36**, 1220–1236, doi:10.1175/JPO2889.1.
- Ray, R. D., and E. D. Zaron, 2011: Non-stationary internal tides observed with satellite altimetry. *Geophys. Res. Lett.*, **38**, L17609, doi:10.1029/2011GL048617.
- Richman, J. G., B. K. Arbic, J. F. Shriver, E. J. Metzger, and A. J. Wallcraft, 2012: Inferring dynamics from the wavenumber spectra of an eddying global ocean model with embedded tides. *J. Geophys. Res.*, **117**, C12012, doi:10.1029/2012JC008364.
- Rocha, C. B., T. Chereskin, S. T. Gille, and D. Menemenlis, 2016: Mesoscale to submesoscale wavenumber spectra in Drake Passage. *J. Phys. Oceanogr.*, **46**, 601–620, doi:10.1175/JPO-D-15-0087.1.
- Shchepetkin, A. F., and J. C. McWilliams, 2005: The Regional Oceanic Modeling System (ROMS): A split-explicit, free-surface, topography-following-coordinate oceanic model. *Ocean Modell.*, **9**, 347–404, doi:10.1016/j.ocemod.2004.08.002.
- Shriver, J. F., J. G. Richman, and B. K. Arbic, 2014: How stationary are the internal tides in a high-resolution global ocean circulation model? *J. Geophys. Res. Oceans*, **119**, 2769–2787, doi:10.1002/2013JC009423.
- Vallis, G. K., 2006: *Atmospheric and Oceanic Fluid Dynamics*. Cambridge University Press, 745 pp.
- Wagner, G. L., 2016: On the coupled evolution of oceanic internal waves and quasi-geostrophic flow. Ph.D. thesis, University of California, San Diego, 216 pp.
- , and W. R. Young, 2016: A three-component model for the coupled evolution of near-inertial waves, quasi-geostrophic flow and the near-inertial second harmonic. *J. Fluid Mech.*, **802**, 806–837, doi:10.1017/jfm.2016.487.
- Ward, M. L., and W. K. Dewar, 2010: Scattering of gravity waves by potential vorticity in a shallow-water fluid. *J. Fluid Mech.*, **663**, 478–506, doi:10.1017/S0022112010003721.
- Xie, J.-H., and J. Vanneste, 2015: A generalised-Lagrangian-mean model of the interactions between near-inertial waves and mean flow. *J. Fluid Mech.*, **774**, 143–169, doi:10.1017/jfm.2015.251.
- Young, W. R., and M. Ben Jelloul, 1997: Propagation of near-inertial oscillations through a geostrophic flow. *J. Mar. Res.*, **55**, 735–766, doi:10.1357/0022240973224283.
- Zaron, E. D., 2015: Non-stationary internal tides observed using dual-satellite altimetry. *J. Phys. Oceanogr.*, **45**, 2239–2246, doi:10.1175/JPO-D-15-0020.1.
- , and G. D. Egbert, 2014: Time-variable refraction of the internal tide at the Hawaiian Ridge. *J. Phys. Oceanogr.*, **44**, 538–557, doi:10.1175/JPO-D-12-0238.1.